fire

MDPI

Article

Evaluation of Integral and Differential Coats–Redfern Methods for Pine Pyrolysis Kinetics

Russell C. Smith and M. Toufiq Reza *

Department of Chemistry and Chemical Engineering, Florida Institute of Technology, 150 W University Boulevard, Melbourne, FL 32901, USA; russell2021@my.fit.edu
* Correspondence: treza@fit.edu

Abstract

This study investigates the pyrolysis behavior of loblolly pine through thermogravimetric (TGA) and derivative thermogravimetric (DTG) analysis under varying nitrogen flow rates of 5–40 mL min^{-1} and heating rates of 5–20 °C min^{-1}. The pyrolysis proceeded through three distinct phases: Phase I: initial moisture release, Phase II: active devolatilization, and Phase III: char formation. Kinetic modeling using both integral and differential forms of the Coats–Redfern method revealed distinct mechanistic interpretations. The integral approach primarily identified diffusion-controlled models (D1, D3) during moisture and char stages and reaction-order or contraction models (F2, R2) during devolatilization, with activation energies ranging from 8.89 to 70.48 kJ mol^{-1}. In contrast, the differential method captured sharper transitions and favored complex nucleation and growth mechanisms (A3, A4) and power laws (P3, P4), yielding higher activation energies up to 111.29 kJ mol^{-1} in Phase II. These results underscore the influence of both inert gas flow and thermal ramp on pyrolysis reactivity and demonstrate that kinetic model selection significantly affects activation energy interpretation. The findings contribute to a more nuanced understanding of biomass pyrolysis and offer insights into reactor design and process optimization in thermochemical conversion systems.

Keywords: biomass; biochar; pyrolysis kinetics; Coats–Redfern; activation energy

1. Introduction

Accurate kinetic modeling of biomass pyrolysis is a cornerstone of thermochemical conversion research, as it provides essential parameters for the design and optimization of reactors that support sustainable energy and material cycles. Pyrolysis is inherently complex, involving the overlapping decomposition of hemicellulose, cellulose, and lignin into gases, condensable volatiles, and solid char [1]. Each of these fractions decomposes over distinct temperature ranges and with characteristic reaction rates, resulting in broad and multistage weight-loss behavior. Reported activation energies for hemicellulose typically fall between 90 and 150 kJ mol^{-1}, while cellulose exhibits sharper devolatilization peaks requiring 180–240 kJ mol^{-1}; lignin, by contrast, decomposes over a wider window of 200–500 °C with activation energies ranging from 30 to greater than 250 kJ mol^{-1} depending on the dominant structure [2–4]. Capturing such heterogeneity demands precise kinetic approaches that can resolve transient mechanisms and account for process variables that strongly influence apparent activation parameters. Thermogravimetric analysis (TGA) is the most widely applied tool for biomass pyrolysis studies because of its ability to provide continuous, high-resolution mass-loss data under controlled temperature programs [5].

Academic Editors: Jakub Čespiva, Jiri Rysavy, Łukasz Niedźwiecki, Yuming Wen and Ruming Pan

Received: 23 January 2026
Revised: 16 February 2026
Accepted: 23 February 2026
Published: 25 February 2026

Numerous investigations have demonstrated that heating rate exerts a primary influence on thermal decomposition behavior [6,7]. For example, increasing the heating rate from 5 to 40 °C min^{-1} has been shown to shift the main devolatilization peak by 15 to 40 °C and increase apparent activation energy estimates by 10 to 30% due to heat and mass transfer limitations [6]. Similarly, biomass type and chemical composition strongly affect both the temperature profile and the kinetic constants, with higher ash or mineral content often retarding devolatilization and promoting char formation through catalytic pathways [8]. Despite this robust body of literature on heating rate and biomass composition, carrier-gas flow effects are better established at the reactor scale (i.e., fluidized and fixed-bed pyrolysis), whereas in lignocellulosic biomass TGA-based kinetic modeling, the purge flow rate is typically reported but not systematically varied, leaving the role of carrier gas flow rate, an equally important operational parameter, under-resolved in terms of its influence on degradation structures, apparent activation energies, and best-fit kinetic models [9,10].

The impact of nitrogen flow rate on pyrolysis kinetics has begun to garner attention in the recent literature. For instance, Brownsort et al. (2009) reported that decreasing flow rates led to enhanced secondary char-forming reactions due to longer vapor residence times, while observing that higher flow rates reduced tar yield by promoting effective vapor-phase sweeping [11]. Still, few studies have systematically incorporated flow rate as a variable in kinetic model-fitting, especially in conjunction with multi-heating rate protocols. Isoconversional approaches such as Kissinger Akahira Sunose (KAS) and Flynn Wall Ozawa (FWO) are commonly applied to biomass TGA to obtain the apparent activation energy as a function of conversion trends, yet they are intentionally model-agnostic and therefore cannot evaluate whether changes in operating conditions shift the best-fit reaction pathway [12]. The Coats–Redfern (CR) method is widely used for non-isothermal solid-state kinetics because it provides phase-resolved apparent activation energy and allows discrimination among candidate reaction-model families (i.e., diffusion, reaction-order, contraction, nucleation) from TGA-DTG data [9,13]. As such, a more rigorous evaluation of how carrier gas flow influences fitted reaction mechanisms and apparent activation energies is urgently needed to align experimental design with industrial relevance.

The CR method exists in two main formulations: integral and differential. The integral form linearizes the Arrhenius equation using conversion data, producing activation energies through regression of $\ln[g(\alpha)/T^2]$ versus $1/T$, where $g(\alpha)$ is the integral conversion function. This approach has the advantage of simplicity and typically generates smoother regression lines, but it may mask localized mechanistic shifts [14]. By contrast, the differential form employs the derivative of conversion $f(\alpha)$, enabling higher sensitivity to localized rate changes and overlapping reactions [15]. However, differential CR often yields higher apparent activation energies and noisier fits. For example, Diana et al. (2025) observed that differential CR produced activation energies for cellulose pyrolysis that were 20% higher than integral CR values, while Gou et al. (2018) reported that different best-fit models emerged depending on which formulation was applied [3,16]. Other studies have corroborated these discrepancies, with differential CR more likely to suggest diffusion-controlled or nucleation mechanisms, whereas integral CR often favors first-order or contracting-geometry models [16]. Despite such findings, very few works have directly compared the two approaches under systematically varied process conditions, such as gas flow rate.

This gap is particularly significant for pine-derived biomass, which often contains substantial ash fractions that alter both chemical reactivity and transport processes during pyrolysis. Accordingly, establishing flow rate-sensitive kinetic behavior in loblolly pine has practical relevance for translating lab-scale TGA kinetics to pine-rich supply chains and thermochemical reactor design [17]. The mineral constituents in pine can catalyze cracking reactions, leading to shifts in volatile release patterns and reductions in apparent

activation energy by 10 to 40 kJ mol^{-1} compared to deashed material [18]. In addition, the presence of ash broadens the derivative thermogravimetric (DTG) peaks, thereby obscuring distinct degradation stages and complicating kinetic model discrimination [19]. When combined with variations in carrier gas flow rate, which influence vapor residence time and secondary reactions, these mineral effects may be further amplified. Under such conditions, reliance on a single Coats–Redfern formulation risks yielding misleading interpretations of activation energies and mechanistic pathways, particularly across sequential moisture, devolatilization, and char stabilization phases characteristic of pine pyrolysis.

The present study addresses this gap by conducting pyrolysis experiments on loblolly pine under five nitrogen flow rates: 5, 10, 20, 30, and 40 mL min^{-1}; and three heating rates: 5, 10, 20 °C min^{-1}. Both integral and differential Coats–Redfern formulations are applied to three distinct thermal phases: phase I, moisture evaporation; phase II, active devolatilization of hemicellulose and cellulose; and phase III, char stabilization and slow lignin degradation, to evaluate the sensitivity of kinetic parameters to gas flow. By systematically comparing activation energies and best-fit models across these conditions, the study clarifies how transport phenomena influence kinetic interpretation and highlights the methodical limitations of CR approaches. The central hypothesis is that purge-gas flow rate systematically biases apparent TGA kinetics by altering vapor sweeping and transport limitations, such that fitted activation energies and best-fit solid-state reaction models differ significantly with flow rate, and that these flow-induced differences are amplified in mineral-rich pine and are not captured consistently by a single CR formulation. Providing a more rigorous insight into selecting purge-flow conditions for biomass pyrolysis and CR formulation when extrapolating laboratory kinetics toward reliable laboratory-to-industrial scaling.

2. Materials and Methods

2.1. Materials

The high ash fraction loblolly pine (LP) was received from Idaho National Laboratory's Biomass Feedstock National User Facility (BFNUF) with particle size < 63 µm. Air classification (AC) was used to separate the low ash fraction and high ash fraction of LP; the higher ash content than the bulk pine is expected. The LPs were oven-dried for 24 h at 105 ± 5 °C. The resulting particles were collected in a Ziplock bag and stored at room temperature. Proper mixing of LP samples was achieved by vigorous manual mixing and used for TG analysis and other characterization methods. For ultimate analysis, vanadium oxide (V_2O_5) and tert-butyl-benoxazol-2-yl thiophene (BBOT) were purchased from Thermo Scientific (Waltham, MA, USA), which were used as sample conditioner and standard, respectively. Tables 1 and 2 display the LP proximate and ultimate analysis.

Table 1. Proximate analysis of LP.

Sample	Moisture Content (wt%)	Volatile Matter Content (wt%)	Ash Content (wt%)	Fixed Carbon Content (wt%)
LP	7.73 ± 0.21	63.19 ± 2.01	12.16 ± 0.02	16.92 ± 1.54

Table 2. Ultimate analysis of LP (b.d. refers to below detection limit).

Sample	Carbon Content (wt%)	Hydrogen Content (wt%)	Nitrogen Content (wt%)	Sulfur Content (wt%)	Oxygen Content (wt%)
LP	42.23 ± 0.01	5.13 ± 0.09	0.80 ± 0.02	b.d.	39.69 ± 0.09

2.2. Biomass Characterization

Loblolly pine (LP) samples were characterized via proximate and ultimate analysis to determine key physicochemical properties. Proximate analysis was performed using a PerkinElmer TGA 4000 (Waltham, MA, USA) to quantify moisture, volatile matter, fixed carbon, and ash contents. Samples were heated under nitrogen at 5 °C min^{-1} from 30 °C to 900 °C, with mass losses at defined stages used to calculate proximate fractions. Ash content was determined separately by combustion in a muffle furnace at 575 °C for 5 h, followed by ASTM D1102 [20]. Ultimate analysis followed ASTM D5373 using a FLASH EA 1112 Series Thermo Scientific (Grand Island, NY, USA), followed by ASTM D5373, where samples were combusted in oxygen and analyzed via a thermal conductivity detector [21]. Oxygen content was calculated by difference. These characterizations supported TGA/DTG-based assessment of thermal reactivity and kinetic modeling.

2.3. Thermogravimetric Analysis

The TG analysis was carried out using a PerkinElmer TGA 4000 (Waltham, MA, USA) as mentioned before. The TG analysis of LP was performed at 5, 10, and 20 °C min^{-1} heating rate as well as 5, 10, 20, 30, and 40 mL min^{-1} nitrogen gas flow rate. LP particles < 63 µm were used to reduce intraparticle heat and internal diffusion limitations common for larger biomass particles in TGA; however, external volatile sweeping, crucible packing effects, and thermal lag can still influence non-isothermal mass-loss profiles. Accordingly, the kinetic parameters reported in this work are interpreted as apparent, phase-resolved kinetics for condition-to-condition comparison rather than strictly intrinsic rate constants. The thermal decomposition behavior and the kinetic parameters for the individual raw materials were studied and compared with respect to the temperature, heat rate, and gas flow rate. The effect of nitrogen gas flow rate on the degradation rate and the kinetic parameters was studied at each heating rate.

2.4. Coats–Redfern Method

The data obtained from TG analysis were used to determine the degradation kinetics of the raw LP using the Coats–Redfern method. The apparent activation energy was calculated using the CR method by linearly model-fitting multiple candidate solid-state reaction models individually; the model families and their corresponding integral and differential forms used are summarized in Table 3. To better represent the complex, multi-step thermal decomposition behavior of lignocellulosic biomass, the overall TG data were segmented into three distinct conversion phases based on the degree of conversion (α). This approach aligns with methodologies adopted in previous studies examining biomass pyrolysis dynamics. Phase I, defined as α = 0.05–0.15, corresponds to the moisture evaporation zone and is dominated by low-temperature physical desorption processes [22]. Phase II, spanning α = 0.20–0.55, represents the active devolatilization stage, during which hemicellulose and cellulose undergo thermal depolymerization and release volatiles [23]. Finally, Phase III, covering α = 0.60–0.95, reflects the charring zone, characterized by biochar stabilization, lignin degradation, and graphitization reactions [24].

To avoid oversimplification, a range of mechanistic models were tested within the CR framework, displayed in Table 3. Reaction order models (Fn) assume random bond scission with nth-order dependence (i.e., F1, F2, F3), while diffusion-controlled models (Dn) describe decomposition limited by one, two, or three-dimensional mass transport. Geometrical contraction models (Rn) represent processes governed by the shrinking core of a particle (i.e., R2 for area and R3 for volume). Nucleation and growth processes were described using the Avrami–Erofeev models (An), which capture the stochastic formation and growth of nuclei during degradation. Finally, power-law models (Pn) were considered to account for early-

stage nucleation and fragmentation behavior. By applying both integral and differential CR formulations across these families, activation energies were extracted for each thermal phase. The combination of statistical fit (R^2) and mechanistic plausibility provided a robust framework for selecting models that best describe the sequential processes of devolatilization and char stabilization during pine pyrolysis.

Table 3. Theoretical Kinetic Models: Integral and Differential.

Model	Integral Form g(α) = kt	Differential Form f(α) = 1/k
Power law (P2)	$\alpha^{1/2}$	$2\alpha^{1/2}$
Power law (P3)	$\alpha^{2/3}$	$3\alpha^{2/3}$
Power law (P4)	$\alpha^{3/4}$	$4\alpha^{3/4}$
Avrami–Erofeev (A2)	$[-\ln(1-\alpha)]^{1/2}$	$2(1-\alpha)\,[-\ln(1-\alpha)]^{1/2}$
Avrami–Erofeev (A3)	$[-\ln(1-\alpha)]^{1/3}$	$3(1-\alpha)\,[-\ln(1-\alpha)]^{2/3}$
Avrami–Erofeev (A4)	$[-\ln(1-\alpha)]^{1/4}$	$4(1-\alpha)\,[-\ln(1-\alpha)]^{3/4}$
Contracting area (R2)	$1-(1-\alpha)^{1/2}$	$2(1-\alpha)^{1/2}$
Contracting volume (R3)	$1-(1-\alpha)^{1/3}$	$3(1-\alpha)^{2/3}$
1D Diffusion (D1)	α^2	$1/(2\alpha)$
2D diffusion (D2)	$[(1-\alpha)\ln(1-\alpha)]+\alpha$	$-[1/\ln(1-\alpha)]$
3D diffusion—Jander (D3)	$[1-(1-\alpha)^{1/3}]^2$	$[3(1-\alpha)^{2/3}]/[2(1-(1-\alpha)^{1/3})]$
First order (F1)	$-\ln(1-\alpha)$	$(1-\alpha)$
Second order (F2)	$[1/(1-\alpha)]-1$	$(1-\alpha)^2$
Third order (F3)	$1/2[(1-\alpha)^{-2}-1]$	$(1-\alpha)^3$

The conversion "α", which represents the mass loss fraction with respect to temperature, can be calculated as:

$$\boldsymbol{\alpha = \frac{W_0 - W_t}{W_0 - W_f}} \quad (1)$$

where W_0 and W_f represent the initial and final mass of the samples in mg, and W_t represents the mass of the sample at any time "t" during thermal degradation.

To begin the kinetic modeling, the fundamental rate law for solid-state decomposition can be expressed as:

$$\boldsymbol{\frac{d\alpha}{dt} = A\ \exp\left(-\frac{Ea}{RT}\right) f(\alpha)} \quad (2)$$

where A is the pre-exponential factor (min^{-1}), Ea is the activation energy (kJ mol^{-1}), T is the temperature in K, t represents time in s, and α represents the mass loss fraction or pyrolysis conversion. f(α) represents the reaction model function. It mathematically represents how the reaction rate depends on the extent of conversion α. This form has been extensively applied in biomass pyrolysis for its simplicity and historical precedent [15,25].

For non-isothermal experiments at a constant heating rate β = dT/dt, the CR method provides two useful linearized forms. The integral CR equation is written as:

$$\boldsymbol{\ln\left(\frac{g(\alpha)}{T^2}\right) = \ln\left(\frac{AR}{\beta Ea}\left(1-\frac{2RT}{Ea}\right)\right) - \frac{Ea}{RT}} \quad (3)$$

where g(α) is the integral form of the chosen kinetic model. A plot of $\ln[g(\alpha)/T^2]$ against 1/T yields a straight line whose slope provides −Ea/R. The integral form is numerically stable because it smooths fluctuations in α, though it can obscure localized mechanistic changes [26].

The differential CR equation is expressed as:

$$\boldsymbol{\ln\left(\frac{f(\alpha)}{T^2}\right) = \ln\left(\frac{AR}{\beta Ea}\right) - \frac{Ea}{RT}} \quad (4)$$

where f(α) represents the differential form of the kinetic model. This formulation uses the instantaneous reaction rate, making it more sensitive to overlapping decomposition events

but also more prone to scatter in the data. In both cases, the approximation (2RT/Ea) < 1 is applied, which holds true for biomass systems where activation energies greatly exceed thermal energy [27]. The CR temperature range is evaluated over the experimental fitting window, not from 0 K. The approximation refers to simplifying this under Ea >> RT. While this generally introduces only a small bias for biomass pyrolysis, it reinforces that CR outputs are apparent parameters and should be interpreted comparatively across conditions within a given phase [28].

3. Results and Discussion

3.1. Thermal Degradation Analysis (TGA/DTG)

Nitrogen flow rate is an important parameter in thermogravimetric pyrolysis experiments because it governs the transport of volatiles away from the reacting biomass. At lower flow rates, the residence time of volatiles in the reaction zone is longer, which enhances secondary reactions such as char formation, repolymerization, and tar cracking. At higher flow rates, volatiles are swept away more rapidly, suppressing secondary pathways and leading to cleaner separation of the primary degradation phases. Since TGA-DTG does not directly quantify condensable tar and permanent gases, product yields are not reported here; however, the flow rate-driven changes in volatile residence time are expected to shift tar-gas pathways and would require TGA-FTIR-MS or separate product-collection analysis to confirm [29]. In this way, nitrogen flow rate directly influences the apparent onset and peak temperatures of thermal events, the shape of DTG peaks, and ultimately the kinetic parameters obtained from model fitting. Understanding its role is therefore essential for interpreting mass loss behavior in relation to pyrolysis kinetics.

The TGA and DTG curves of LP are shown in Figure 1a–e. The pyrolysis trends at each heat rate were almost analogous. The rate of mass loss increased with an increase in heating rate, as observed from DTG peaks. In addition to heating rate, nitrogen flow rate plays a critical role because it modulates gas–solid interactions and determines the extent to which transport limitations influence the observed degradation profile. The initial mass loss was about 10% due to the evaporation of moisture, which started at around 80 °C and continued up to 150 °C at all rates of heating, representing phase I. The decomposition of lignocellulosic materials such as hemicellulose, cellulose, and lignin took place in two steps, which were observed at around 180–414 °C and 414–511 °C, where hemicellulose and cellulose were observed in the first peak and lignin in the second peak, both in phase II. The overlapping of peaks of the corresponding lignocellulose decomposition was also evident from the literature [29]. The further decomposition of lignocellulosic biomass after hemicellulose, cellulose, and lignin are removed from the material biomass undergoes a charring mechanism phase III peak from 511 to 900 °C. The maximum mass loss rate changed with different heat rates as well as nitrogen gas flow rates. It was observed that at 5 °C min^{-1}, the temperature at maximum mass loss occurred at 315, 313, 315, 316, 317 °C at 5, 10, 20, 30, and 40 mL min^{-1}, respectively. At 10 °C min^{-1}, the temperature at maximum mass loss occurred at 333, 332, 334, 336, and 338 °C at 5, 10, 20, 30, and 40 mL min^{-1}, respectively. At 20 °C min^{-1}, the temperature at maximum mass loss occurred at 358, 357, 363, 363, and 360 °C at 5, 10, 20, 30, and 40 mL min^{-1}, respectively. The general trend observed was that with an increase in heat rate, there is a greater significance of nitrogen gas flow rate plays on the maximum mass loss rate. The effect nitrogen gas flow rate plays on the degradation of lignocellulosic biomass is that with a greater gas flow rate, higher temperatures are required to obtain the maximum mass loss rate of phase II, the degradation of hemicellulose and cellulose. At higher heating rates, the TGA-DTG features broadened and shifted to higher temperatures, which is consistent with thermal lag, i.e., the programmed furnace temperature increases faster than the sample

can reach thermal equilibrium, creating transient temperature gradients within the sample and delaying the observed mass-loss response [7,30]. In addition, the DTG peak height increased with heating rate because the mass-loss event is compressed into a shorter time window, increasing the mass-loss rate even when the temperature domain profile changes only modestly [31]. Accordingly, heating rate primarily affects peak position and width through thermal lag and time-compression, whereas nitrogen flow rate governs volatile sweeping and the extent of secondary reactions by residence-time and mass-transfer effects.

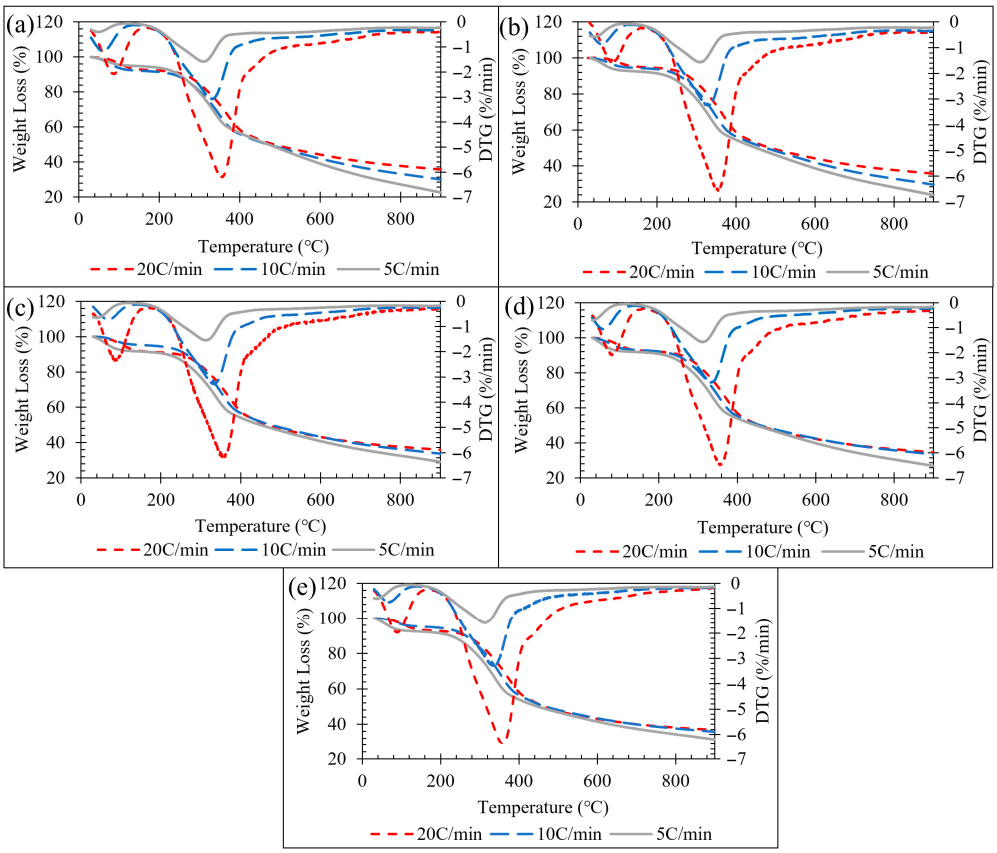

Figure 1. (**a**) 5 mL min^{-1} TGA-DTG, (**b**) 10 mL min^{-1} TGA-DTG, (**c**) 20 mL min^{-1} TGA-DTG, (**d**) 30 mL min^{-1} TGA-DTG, (**e**) 40 mL min^{-1} TGA-DTG.

Figure 2a–c shows the TGA and DTG curves at each nitrogen gas flow rate and heat rate, respectively. The largest effect nitrogen gas flow rate plays on lignocellulosic biomass was with low heat rates 5 and 10 °C min^{-1} while higher heating rates, i.e., 20 °C min^{-1} nitrogen gas flow rate plays a smaller role, meaning that varying the purge flow from 5 to 40 mL min^{-1} produces only minor changes in the TGA-DTG response peak position and most notably, the extent of phase III mass loss, because the faster temperature ramp compresses the devolatilization event in time and heating rate driven thermal lag dominates relative to flow-dependent volatile sweeping and secondary-reaction effects. This nitrogen gas flow rate dependence was observed especially in Figure 2a, with a heat rate of 5 °C min^{-1} greater mass loss occurred in phase III for 5 mL min^{-1}, and the least mass loss in phase III for 40 mL min^{-1}. The greater total mass loss at low heat rates, i.e., 5 °C min$^{-1,}$ with lower nitrogen gas flow rates, i.e., 5 mL min^{-1} was likely due to the system having more time for heat transfer and gas–solid interactions to occur. Lower nitrogen flow rates, i.e., 5 mL min^{-1} create a stagnant environment leading to possibilities for partial oxidation, accumulation of volatiles, more dominant secondary reactions (char formation and repolymerization), and prolonged mass loss in phase III associated with char degradation. The fixed carbon content in the heat rate 5 °C min^{-1} decreases as nitrogen flow rates

decrease, indicating that slower purge conditions allowed additional char consumption during the high-temperature phase III region, leaving less solid residue at the end of the run. While the heat rate of 20 °C $min^{-1,}$ Figure 2c shows the minimal mass loss vs. gas flow rate dependence on the system in each phase of degradation. Higher nitrogen flow rates, i.e., 40 mL $min^{-1,}$ rapidly sweep away volatiles, which suppresses secondary reactions, leading to the system focusing on the primary degradation phases I and II only. Literature reveals that if lignocellulosic biomass is heated quickly, i.e., 20 °C min^{-1} thermal gradients dominate, residence time of volatiles is smaller regardless of nitrogen flow rate, and mass loss is more kinetic-controlled than influenced by flow-dependent transport effects [32–35]. This confirmed that the total mass loss of lignocellulosic biomass is dependent on nitrogen gas flow rate at moderate to slow heating rates, 5 to 10 °C min^{-1}, in parallel with heat rate.

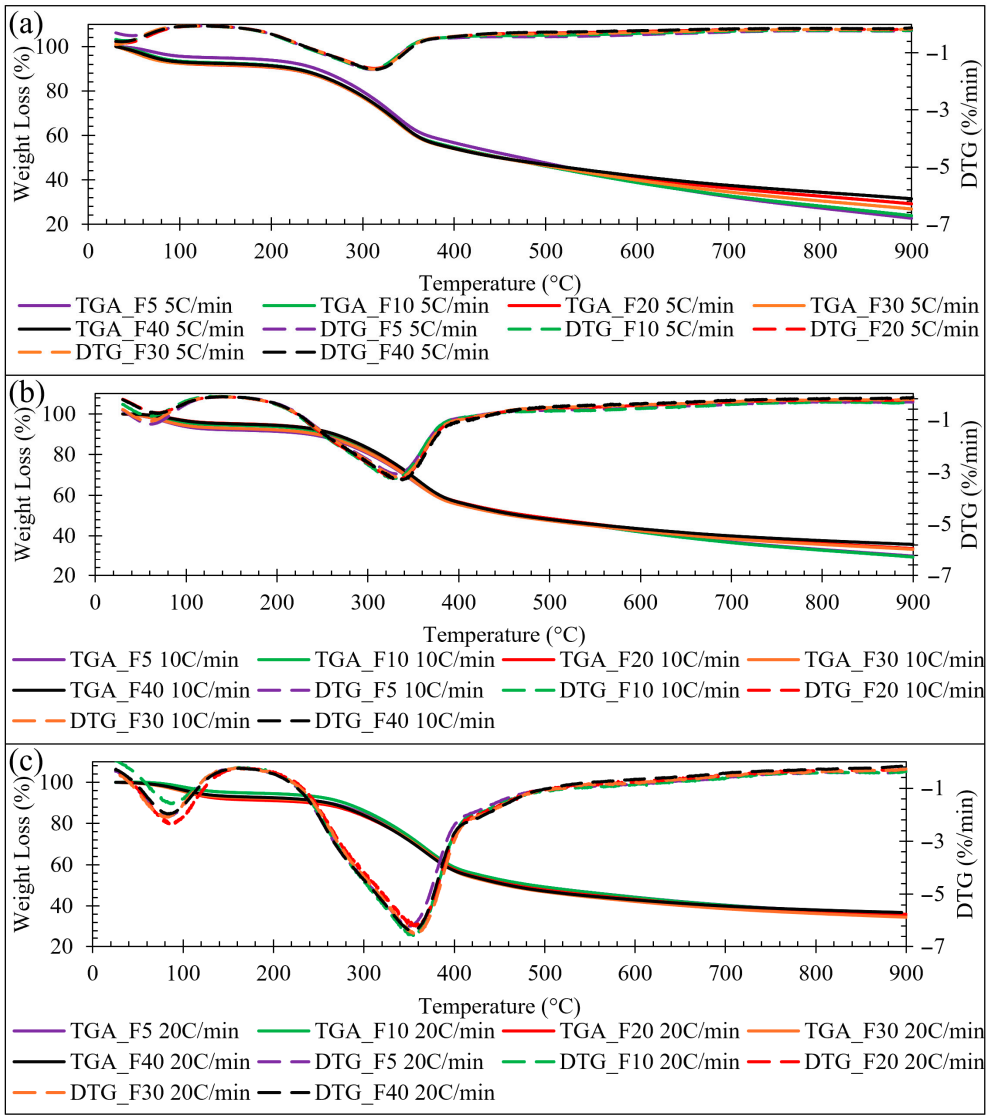

Figure 2. (**a**) TGA-DTG 5 °C min^{-1} gas flow rates, (**b**) TGA-DTG 10 °C min^{-1} gas flow rates, (**c**) TGA-DTG 20 °C min^{-1} gas flow rates.

3.2. Kinetic Analysis by Integral Coats–Redfern Method

The integral Coats–Redfern method provided a macro-scale kinetic assessment of LP pyrolysis by evaluating the cumulative conversion function, g(α), across different nitrogen flow rates and heating rates. This method is particularly advantageous in identifying overarching kinetic behavior by smoothing transient variations, allowing for robust detection

of dominant reaction mechanisms across extended temperature windows. The best-fitted model correlating to each process optimization is displayed in Table 4. In this context, process optimization refers to the selection of the most appropriate kinetic model for each combination of heating rate, nitrogen flow rate, and degradation phase by identifying the integral CR model that yielded the highest correlation coefficient R^2. Since DTG peaks are broad and overlapping, changes in the best-fit CR mechanism family do not necessarily correspond to an abrupt, visually distinct DTG peak-shape change. Thus, the integral CR mechanism selection is interpreted as the apparent controlling regime that best linearizes the data over the chosen phase conversion window, rather than a unique DTG mechanistic fingerprint. While TGA is a laboratory-scale technique, these results can guide process optimization at larger scales by indicating which operating conditions minimize secondary reactions, enhance volatile release, or stabilize char formation. For example, the identification of higher activation energies under certain flow rates suggests transport limitations that could be mitigated by adjusting carrier gas supply in a reactor, whereas models showing improved fits under specific heating rates can inform temperature ramping strategies in industrial systems. Thus, TGA–derived kinetic parameters provide a foundational basis for optimizing reactor design and operating conditions in thermochemical conversion.

Table 4. Determination of the model, activation energy with respect to the correction factor (R^2), integral method.

Sample	Mechanism	Activation Energy /kJ mol^{-1}	R^2 Value	Mechanism	Activation Energy/kJ mol^{-1}	R^2 Value	Mechanism	Activation Energy /kJ mol^{-1}	R^2 Value
		Phase I			Phase II			Phase III	
5 mL min^{-1}									
5 °C min^{-1}	D1	11.46	0.8605	F2	35.57	0.9755	D3	14.53	0.9931
10 °C min^{-1}	D3	11.44	0.6916	D1	51.76	0.9997	D3	10.51	0.9928
20 °C min^{-1}	D3	13.59	0.7117	D1	57.04	0.9999	F2	22.73	0.9706
10 mL min^{-1}									
5 °C min^{-1}	D3	12.06	0.9998	D3	59.00	0.9971	D3	11.67	0.9908
10 °C min^{-1}	D1	11.51	0.8949	D3	70.48	0.9996	D3	11.00	0.9955
20 °C min^{-1}	D1	14.42	0.9238	R2/R3/D3	32.33/33.98/78.08	0.9999	F2	23.25	0.9718
20 mL min^{-1}									
5 °C min^{-1}	D3	10.14	0.6263	D1	48.47	0.9994	D3	9.13	0.9923
10 °C min^{-1}	D1	13.22	0.8936	R2/R3/D2	30.63/32.30/67.94	0.9999	D3	10.58	0.9614
20 °C min^{-1}	D3	12.37	0.9336	D1	52.68	0.9993	F2	24.58	0.9829
30 mL min^{-1}									
5 °C min^{-1}	D3	9.45	0.6569	D1	49.20	0.9992	D3	9.99	0.9916
10 °C min^{-1}	D3	12.20	0.7944	D1	54.37	0.9999	F2	20.14	0.9607
20 °C min^{-1}	D3	12.84	0.7143	D1	57.03	0.9999	F2	24.23	0.9817
40 mL min^{-1}									
5 °C min^{-1}	D3	10.31	0.6830	D1	50.84	0.9995	D3	12.94	0.9220
10 °C min^{-1}	D1	12.91	0.9043	D2	68.22	1.0000	F2	22.05	0.9793
20 °C min^{-1}	D3	14.33	0.7526	D1	58.57	1.0000	F2	27.23	0.9880

In Phase I, corresponding to moisture evaporation, Ea values ranged from 8.89 to 14.42 kJ mol^{-1}. At a low flow rate of 5 mL min^{-1} and heating rate 5 °C min^{-1}, the D3 model offered the best fit, with Ea of 8.89 kJ mol^{-1}. This is characteristic of moisture transport through porous biomass matrices [36]. As heating rates increased, Ea values showed a slight rise, up to 14.42 kJ mol^{-1}, indicating enhanced vaporization driven by higher thermal gradients. Interestingly, increasing the nitrogen flow rate to 40 mL min^{-1} led to marginally elevated Ea values, yet D3 remained dominant. This suggests that higher sweeping rates expedite water vapor removal and reduce boundary layer resistance, thus maintaining diffusion-limited desorption as the governing mechanism while slightly increasing the energy required for thermal dehydration due to shortened resistance times. Similar trends have been reported in the literature. Congxiao et al. (2023) observed that higher carrier

gas flow rates facilitated more effective vapor removal during biomass pyrolysis, leading to reduced secondary condensation but slightly higher apparent activation energies for early-stage mass loss [37]. This indicates that while the persistence of diffusion-controlled mechanisms during dehydration is widely observed, the magnitude of Ea shifts with flow rate can vary depending on biomass type and porosity, with pine exhibiting a modest sensitivity to carrier gas velocity.

In Phase II, kinetic complexity increased markedly. Ea values ranged from 30.63 to 70.48 kJ mol^{-1} and varied significantly with both heat rate and flow rate. Ea rises in Phase II because this region captures the primary devolatilization, which is inherently more energy-demanding than moisture loss and early-stage reactions. At 5 °C min^{-1}, D1 and F2 models were dominant, representing a slow diffusion-limited devolatilization regime. As the heat rate increased to 10 and 20 °C min^{-1}, mechanisms transitioned to mixed forms (R2, R3, D1, D3), and Ea values rose accordingly. These shifts suggest a stronger influence of bond-breaking reactions under elevated thermal energy [18]. Notably, at intermediate flow rates 10 and 20 mL min^{-1}, the highest Ea values were recorded, indicating an optimal gas–solid interaction window for maximum conversion efficiency. At 40 mL min^{-1} and 20 °C min^{-1}, however, a return to D1 was observed with an Ea of 68.22 kJ mol^{-1}, implying that excessive gas sweeping limits thermal coupling and suppresses secondary reactions [11].

In Phase III, Ea values ranged from 6.67 to 27.23 kJ mol^{-1} and were generally lower than those in Phase II, consistent with a slow char formation process. At 5 °C min^{-1}, D3 mechanisms were dominant across flow rates, highlighting diffusion-limited restructuring. As the flow rate increased, Ea also increased, underscoring the influence of inert gas on reaction progression. At 10 and 20 °C min^{-1}, F2 mechanisms emerged at higher flow rates of 30 and 40 mL min^{-1}, suggesting a shift to reaction-controlled pathways driven by aromatic condensation [38]. The maximum Ea observed was 27.23 kJ mol^{-1} at 40 mL min^{-1}, and 20 °C min^{-1}, associated with strong F2 fits and minimal char reactivity. Conversely, low flow rate and low heat rate conditions showed minimum Ea values, with D3 models indicative of an optimal thermal environment for stable char production.

Collectively, the integral Coats–Redfern method captured phase-averaged kinetic trends that are crucial for process scaling and reactor design. It showed that nitrogen flow rate and heating rate jointly control the activation energy landscape of LP pyrolysis. The method excelled in identifying the dominant mechanisms and averaged energy barriers across phases, though it was less sensitive to localized kinetic transitions. Importantly, optimal devolatilization was observed at 10 to 20 mL min^{-1} and 10 to 20 °C min^{-1}, where a balance of heat and mass transfer facilitated maximum energy release and volatile evolution. By contrast, low flow rates favored complete degradation but prolonged reaction time, while high flow rates suppressed char burnout. These findings emphasize the utility of integral modeling for thermochemical optimization, especially when designing pyrolysis systems targeting steady-state operation and energy efficiency in biomass conversion.

3.3. Kinetic Analysis by Differential Coats–Redfern Method

The differential Coats–Redfern method offered phase insights into the pyrolytic behavior of LP by analyzing the temperature derivative of conversion, f(α), enabling sharper phase-specific kinetic characterization across various nitrogen flow rates and heating rates. This method's sensitivity to instantaneous reaction rates provided more accurate estimates of the true activation energies and mechanistic transitions that occurred during each pyrolysis phase. The best-fitted model correlating to each process optimization is displayed in Table 5.

Table 5. Determination of the model, activation energy with respect to the correction factor (R^2), differential method.

Sample	Mechanism	Activation Energy /kJ mol^{-1}	R^2 Value	Mechanism	Activation Energy /kJ mol^{-1}	R^2 Value	Mechanism	Activation Energy /kJ mol^{-1}	R^2 Value
		Phase I			Phase II			Phase III	
5 mL min^{-1}									
5 °C min^{-1}	P4	22.88	0.9791	P4	78.29	0.9679	A4	11.10	0.9030
10 °C min^{-1}	P4	20.94	0.9076	P3	51.76	0.9997	P4	7.33	0.9355
20 °C min^{-1}	A4	23.54	0.7742	P2-P4	23.51–89.91	0.9999	P4	5.59	0.7259
10 mL min^{-1}									
5 °C min^{-1}	P4/A4	20.63/21.06	0.9999	A4	84.85	0.9962	P4	6.63	0.9302
10 °C min^{-1}	P4	20.84	0.9230	A4	100.74	0.9991	P4	6.09	0.8719
20 °C min^{-1}	P4	25.40	0.9416	A4	111.29	0.9998	P4	6.86	0.6311
20 mL min^{-1}									
5 °C min^{-1}	A4	18.17	0.7139	A3	47.16	0.9995	P4	4.61	0.7727
10 °C min^{-1}	P4	23.48	0.9197	A4	106.01	0.9999	P4	5.62	0.6687
20 °C min^{-1}	A4	21.53	0.8769	A3	51.28	0.9995	P4	7.31	0.5617
30 mL min^{-1}									
5 °C min^{-1}	A4	17.15	0.7464	P4	78.62	0.9993	P4	5.34	0.8886
10 °C min^{-1}	A4	21.34	0.8471	A4	108.86	1.0000	P4	5.02	0.7883
20 °C min^{-1}	P4	21.62	0.7848	P2/P3 /P4/A3	23.51/57.03 /90.34/55.51	0.9999	A4	8.88	0.5465
40 mL min^{-1}									
5 °C min^{-1}	P4	18.62	0.7717	A3	49.48	0.9997	A4	10.10	0.9107
10 °C min^{-1}	P4	23.92	0.9937	A4	106.41	1.0000	P4	7.41	0.8576
20 °C min^{-1}	P4	24.78	0.9140	P3	58.57	1.0000	A4	10.38	0.5464

In Phase I, which corresponds to the initial moisture evaporation and bound water release occurring, the Ea values ranged from 17.15 to 25.40 kJ mol^{-1} across all conditions. At the lowest flow rate of 5 mL min^{-1} and heating rate of 5 °C min^{-1}, the power low model P4 best described the kinetic behavior, yielding an Ea of 22.88 kJ mol^{-1} with a strong R^2 value of 0.9791. As the heating rate increased to 10 °C min^{-1}, the Ea slightly decreased to 20.94 kJ mol^{-1} with a reduced R^2 of 0.9076, reflecting the onset of more rapid desorption. At 20 °C min^{-1}, the mechanism shifted to A4, representing Avrami–Erofeev–type nucleation with an Ea of 23.54 kJ mol^{-1}, although the fit weakened R^2 of 0.7742 due to increased volatility. As the nitrogen flow rate increased to 10 mL min^{-1}, the kinetic behavior remained governed by P4 and A4, with Ea values ranging from 20.63 to 25.40 kJ mol^{-1}. This suggests a balance between thermal driving force and vapor removal efficiency. At even higher flow rates of 20, 30, and 40 mL min^{-1}, the Ea values slightly decrease, falling to as low as 17.15 kJ mol^{-1}, while the dominant mechanisms continued to favor P4 or A4, indicating that increased inert sweeping enhanced moisture evacuation, reducing the partial pressure and promoting more effective mass transport during drying [36]. It should be noted that the variation in Ea values within the same phase reflects the sensitivity of the differential Coats–Redfern method to local variations in the f(α). Because moisture release in pine involves both free and bound water, as well as interactions with the porous matrix, the process is not governed by a single, sharp transition but by overlapping desorption events. As a result, the differential method captures small shifts in peak transition and slope as experimental conditions change, producing modest variations in apparent activation energy even within the same moisture–evaporation phase. Similar ranges have been reported in previous TGA studies of biomass drying, where Ea values for moisture release typically span 10–30 kJ mol^{-1}, depending on flow rate and heating rate [14].

The most significant kinetic transitions were observed in Phase II, where devolatilization of hemicellulose and cellulose occurs, often accompanied by tar evolution and sec-

ondary cracking. Activation energies varied widely from 23.51 to 111.29 kJ mol^{-1}, depending on gas flow rate and heating rate. At 5 mL min^{-1} and 5 °C min^{-1}, the P4 model provided the best fit, with an Ea of 78.29 kJ mol^{-1}, signifying a high-order reaction consistent with gradual thermal degradation. As the heating rate increased to 10 °C min^{-1}, the mechanism shifted to P3, and Ea decreased to 51.76 kJ mol^{-1}, while model fit improved, indicating accelerated devolatilization under higher thermal input, At 20 °C min^{-1}, the best fit spanned a range of power law models P2, P3, and P4, with Ea values spanning from 23.51 to 89.91 kJ mol^{-1}, illustrating the coexistence of rapid fragmentation and delayed decomposition reaction at high ramping speeds [39]. At 10 mL min^{-1}, the Avrami–Erofeev nucleation model A4 consistently emerged as the best fit at both 10 and 20 °C min^{-1}, with Ea values of 100.74 and 111.29 kJ mol^{-1}, respectively, among the highest observed. These results underscore that intermediate gas flow and moderate heating create favorable conditions for nucleation-dominated mechanisms, where the buildup and propagation of reactive intermediates proceed through organized structural transitions. Similarly, at 20 mL min^{-1}, A3 and A4 dominated, with Ea values remaining above 100 kJ mol^{-1}, signifying an optimal kinetic environment for intensive devolatilization without immediate sweeping of volatiles. In contrast, at 40 mL min^{-1} and 20 °C min^{-1}, Ea decreased to 58.57 kJ mol^{-1} P3, suggesting that excessive inert gas flow may suppress slower secondary cracking reactions by prematurely evacuating volatile fragments. This indicates a critical flow threshold beyond which reactive residence time diminishes, lowering the observed energy barriers and reverting reaction mechanisms to lower-order forms.

This trend aligns with published literature. Tariq et al. (2023) and Raza et al. (2023) reported similar heating rate effects on pyrolysis, noting enhanced mass loss and secondary reactions at lower rates and more kinetic-dominated pathways at higher rates [40,41]. Activation energies for biomass devolatilization reported in the literature typically range from 30–120 kJ mol^{-1}, with high-ash feedstocks often showing reduced Ea values in char-forming stages due to catalytic mineral content [42].

In Phase III, which represents the slow aromatization and restructuring of residual biomass into char, the Ea values were the lowest, ranging from 4.61 to 11.10 kJ mol^{-1} across all tested conditions. At 5 mL min^{-1} and 5 °C min^{-1}, the A4 model best described the charring process, with an Ea of 11.10 kJ mol^{-1} and a moderate fit, indicative of a nucleation-driven carbonization regime. Increasing the heating rate to 10 and 20 °C min^{-1} led to a transition toward P4, with decreasing Ea values of 7.33 and 5.59 kJ mol^{-1}, respectively, and reduced fitted values. This suggests that faster heating compresses the charring window, leading to more disordered condensation of residual aromatics. As flow rate increased, particularly at 30 and 40 mL min^{-1}, the Ea remained relatively stable, though fit quality deteriorated at 20 °C min^{-1}, likely due to the less uniform nature of char-forming reactions under high sweep conditions. The highest Ea in Phase III, 10.38 kJ mol^{-1}, was observed at 40 mL min^{-1} and 20 °C min^{-1}, modeled by A4, suggesting that under rapid ramping and vigorous gas flow, charring remains nucleation-dominated but proceeds through faster, less ordered pathways.

Altogether, the differential Coats–Redfern method effectively captured the nuanced kinetic responses of LP pyrolysis to variations in nitrogen flow and temperature. The method revealed that intermediate flow rates of 10 and 20 mL min^{-1} and a moderate heating rate of 10 °C min^{-1} promoted the highest activation energies and mechanistic complexity, particularly in Phase II. In contrast, low flow and low heating rate favored more stable, diffusion-limited regimes, while excessively high flow and ramping suppressed secondary transformations, leading to simplified kinetic behavior. This detailed kinetic mapping underscores the importance of process parameter optimization to tailor product selectivity, whether for maximizing volatile production in energy applications or high-

producing high-yield char. Table 6 indicates that the kinetic properties of loblolly pine are comparable to those of other biomass materials reported in the literature. Specifically, the activation energies determined for loblolly pine 4.61–111.29 kJ mol^{-1} fall within the broader ranges observed for various lignocellulosic feedstocks. For example, pinewood pellets analyzed by Mian et al. reported Ea values between 120 and 210 kJ mol^{-1}, sugarcane residue by Song et al. ranged from 23 to 63 kJ mol^{-1}, while plywood and Douglas fir exhibited even wider spans up to 336 kJ mol^{-1}. The pre-exponential factors for loblolly pine also overlap with those reported for date palm fibers, plywood, and oil-palm residues, further supporting the consistency of these results. Mechanistically, the dominance of nucleation-growth, diffusion, and power-law models in this study aligns with findings for ramie fabric waste, cellulose, and Douglas fir, where similar models have been identified. Collectively, this comparison confirms that loblolly pine behaves similarly to other woody and herbaceous biomasses under TGA conditions, with kinetic variability largely reflecting differences in composition, ash content, and heating or flow rate regimes. Thus, the present study reinforces that the observed Ea and mechanistic pathways are not anomalous but rather consistent with established biomass pyrolysis literature.

3.4. Criteria-Based Comparison of Integral vs. Differential Coats–Redfern

To assess the usefulness of the integral and differential CR formulations for LP TGA under varying nitrogen gas flow and heating rate, these were compared using four practical criteria, first, regression stability (R^2 consistency), second, robustness of extracted kinetic parameters across operating conditions within each phase, third, phase-consistency and interpretability of the inferred mechanism families, and fourth, suitability for the intended application trend mapping vs. transition detection. Overall, the integral CR formulation produced smoother linear regressions and more stable phase Ea trends across alternating nitrogen gas flow rate and heating rate combinations, making it better suited for benchmarking and for constructing a sensitivity map of how operating conditions bias apparent kinetics. In contrast, the differential CR formulation was more sensitive to localized rate changes and overlapping devolatilization behavior, often selecting nucleation or power-law mechanisms and yielding higher Ea in Phase II, which is valuable for identifying potential mechanistic transitions but also reflects greater sensitivity to experimental noise and peak overlap. Therefore, for reactor-relevant parameter screening and comparative reporting across conditions, integral CR is recommended as the primary estimator, while differential CR is most useful as a complementary diagnostic to highlight where formulation choice and overlap or transport artifacts may alter mechanistic interpretation, particularly in Phase II devolatilization of biomass. A phase-by-phase practical summary of these strengths, limitations, and recommended uses is provided in Table 7. Finally, it should be noted that CR is a model-fitting linearization applied over a selected conversion window and therefore yields apparent phase parameters in a multi-step pyrolysis system. High R^2 does not guarantee mechanistic uniqueness, and fitted apparent Ea or model selection can vary with conversion window choice, peak overlap, and transport artifacts, i.e., thermal lag and volatile sweeping. In the biomass TGA literature, these issues are often addressed by pairing model fitting with model-free isoconversional methods (FWO, KAS, Friedman) that provide activation energy as a function of conversion, or with multi-step models such as DAEM that better represent overlapping reactions [43–45]. Accordingly, the present CR results are used for condition-to-condition comparison and sensitivity mapping rather than claiming unique intrinsic kinetics.

Table 6. Past Literature on pyrolysis kinetics and their reported Ea and reaction mechanisms (N.R. refers to not recorded in manuscript).

TGA Studies	Material	Method	E_a (kJ mol^{-1})	Conversion (α)	Reaction Mechanism/Order	Reference
Mian et al.	Pinewood pellets	Nonisothermal @ 3–10 °C min^{-1}, 100 mL min^{-1}, Integral Coats–Redfern	120.58–210.55	0.1–0.9	No mechanism or order stated	[13]
Chen et al.	Industrial lignin	Nonisothermal @10–30 °C min^{-1}, 50 mL min^{-1}, Integral Coats–Redfern	21.37–26.70	0.20–0.90	No mechanism or order stated	[14]
Song et al.	Sugar cane residue	Nonisothermal @10 °C min^{-1}, 60 mL min^{-1}, Integral Coats–Redfern	23.01–60.53	N.R.	Only first-order evaluated	[46]
Zhu et al.	Ramie fabric wastes	Nonisothermal @ 5, 10, 20, and 40 °C min^{-1}, 50 mL min^{-1}, Differential Coats–Redfern	156.40–231.80	0.10–0.75	R2 and R3	[47]
Kumar et al.	Plywood	Nonisothermal @ 5–100 K min^{-1}, 200 mL min^{-1}, Integral Coats–Redfern	44.32–200.82	N.R.	Only reaction order mechanisms evaluated	[48]
Wang et al.	Cellulose, hemicellulose, and lignin	Nonisothermal @ 5–40 °C min^{-1}, 40 mL min^{-1}, Integral and Differential Coats–Redfern	91.0–439.4	0.05–0.95	A2	[49]
Wang et al.	Douglas fir	Nonisothermal @ 10–40 °C min^{-1}, 20 mL min^{-1}, Integral Coats–Redfern	78.15–336.30	0.20–0.70	Only reaction order mechanisms evaluated	[26]
Postawa et al.	Waste plant (Stalks, Leaves, Whole plant)	Nonisothermal @ 2 °C min^{-1}, 5 mL min^{-1}, Integral Coats–Redfern	3.30–71.60	N.R.	Many possible mechanisms	[50]
Surahmanto et al.	Oil-palm solid waste	Nonisothermal @ 10 °C min^{-1}, 10 mL min^{-1}, Integral Coats–Redfern	7.95–63.25	N.R.	Only first-order evaluated	[27]
Ali et al.	Malaysian wood (Hardwood, Medium hardwood, and Light hardwood)	Nonisothermal @ 5–20 °C min^{-1}, 50 mL min^{-1}, Integral Coats–Redfern	27.26–55.94	N.R.	Only first-order evaluated	[51]
Raza et al.	Date palm surface fibers	Nonisothermal @ 10 °C min^{-1}, 60 mL min^{-1}, Integral Coats–Redfern	0.60–166.91	N.R.	Many possible mechanisms	[41]
Smith et al.	Loblolly pine	Nonisothermal @ 5–20 °C min^{-1}, 5–40 mL min^{-1}, Integral and Differential Coats–Redfern	4.61–111.29	0.05–0.95	Many possible mechanisms	This study

Table 7. Comparison of integral and differential Coats–Redfern formulations for lignocellulosic biomass TGA.

Phase	Integral CR: Strengths/Limitations	Differential CR: Strengths/Limitations	Recommended Use
Phase I (moisture release)	**Strengths:** smoother regressions, robust phase Ea trends, less sensitive to small fluctuations in conversion. **Limitations:** may mask minor shifts between free vs. bound water release.	**Strengths:** can detect subtle local slope changes in early mass loss. **Limitations:** more noise-sensitive, may over-emphasize small rate variations and yield higher scatter in fitted parameters.	Use integral CR for primary reporting since stable dehydration kinetics; use differential CR only as a diagnostic if early-stage transitions are of interest.
Phase II (active devolatilization)	**Strengths:** stable phase kinetics useful for comparing operating conditions. **Limitations:** smoothing can obscure localized mechanistic transitions during overlapping reactions.	**Strengths:** high sensitivity to localized rate changes and overlap, highlights potential mechanistic transitions, often identifies nucleation or power-law behavior during rapid devolatilization. **Limitations:** more susceptible to peak overlap and experimental noise, can produce higher apparent Ea and more model switching.	Report integral CR as the benchmark for condition-to-condition comparisons; use differential CR to interrogate transitions or overlap and to bracket uncertainty in apparent Ea and mechanism selection.
Phase III (char stabilization)	**Strengths:** robust for slow, diffusion or structural rearrangement-dominated behavior, good for comparing char-stage trends across gas flow rate. **Limitations:** may under-resolve short-lived late-stage events.	**Strengths:** can highlight localized changes in slow tailing region. **Limitations:** low DTG signal and noise can dominate, fits may be less reliable and more scattered.	Prefer integral CR for char-stage kinetics and trend mapping; use differential CR cautiously and primarily for qualitative confirmation of localized changes.

4. Conclusions

The pyrolysis behavior of high ash fraction loblolly pine (LP) under varying nitrogen flow rates 5, 10, 20, 30, and 40 mL min^{-1} and heating rates 5, 10, and 20 °C min^{-1} was systematically investigated through thermogravimetric analysis and Coats–Redfern kinetic modeling. Thermal decomposition was segmented into three phases: moisture release (Phase I), devolatilization (Phase II), and char formation (Phase III). Lower flow rates and heating rates promoted greater mass loss >80% due to enhanced residence time and secondary reactions, while higher flow rates and heat rates increased DTG peak temperatures 315–365 °C, indicating thermal lag. The integral Coats–Redfern method revealed dominant diffusion mechanisms D3 in Phase I and reaction-order or contraction models in Phase II, with optimal devolatilization at moderate flow and heating rates. The differential method captured sharper transitions, especially in Phase II, identifying Avrami–Erofeev and power-law mechanisms with higher Ea values. Based on regression stability and parameter robustness across operating conditions, integral CR is recommended for phase kinetic benchmarking and trend mapping, while differential CR is best used as a diagnostic tool to interrogate localized transitions and overlap effects. Together, these findings highlight the critical role of gas–solid interactions and support informed design of pyrolysis systems.

Author Contributions: Conceptualization, M.T.R. and R.C.S.; methodology, M.T.R. and R.C.S.; validation, M.T.R. and R.C.S.; formal analysis, R.C.S.; investigation, R.C.S.; writing—original draft preparation, R.C.S.; writing—review and editing, M.T.R. and R.C.S.; visualization, M.T.R.; supervision, M.T.R.; project administration, M.T.R. All authors have read and agreed to the published version of the manuscript.

Funding: This research received no external funding.

Institutional Review Board Statement: Not applicable.

Informed Consent Statement: Not applicable.

Data Availability Statement: Data will be made available on request.

Acknowledgments: All authors have reviewed and edited the output and take full responsibility for the content of this publication.

Conflicts of Interest: The authors declare no conflicts of interest.

References

1. Chen, D.; Cen, K.; Zhuang, X.; Gan, Z.; Zhou, J.; Zhang, Y.; Zhang, H. Insight into biomass pyrolysis mechanism based on cellulose, hemicellulose, and lignin: Evolution of volatiles and kinetics, elucidation of reaction pathways, and characterization of gas, biochar and bio-oil. *Combust. Flame* **2022**, *242*, 112142. [CrossRef]
2. Yeo, J.Y.; Chin, B.L.F.; Tan, J.K.; Loh, Y.S. Comparative studies on the pyrolysis of cellulose, hemicellulose, and lignin based on combined kinetics. *J. Energy Inst.* **2019**, *92*, 27–37. [CrossRef]
3. Gou, X.; Zhang, Q.; Liu, Y.; Wang, Z.; Zou, M.; Zhao, X. A novel method of kinetic analysis and its application to pulverized coal combustion under different oxygen concentrations. *Energies* **2018**, *11*, 1799. [CrossRef]
4. Díez, D.; Urueña, A.; Piñero, R.; Barrio, A.; Tamminen, T. Determination of hemicellulose, cellulose, and lignin content in different types of biomasses by thermogravimetric analysis and pseudocomponent kinetic model (TGA-PKM method). *Processes* **2020**, *8*, 1048. [CrossRef]
5. Yang, X.; Zhao, Y.; Li, W.; Li, R.; Wu, Y. Unveiling the pyrolysis mechanisms of hemicellulose: Experimental and theoretical studies. *Energy Fuels* **2019**, *33*, 4352–4360. [CrossRef]
6. Mehrabian, R.; Scharler, R.; Obernberger, I. Effects of pyrolysis conditions on the heating rate in biomass particles and applicability of TGA kinetic parameters in particle thermal conversion modelling. *Fuel* **2012**, *93*, 567–575. [CrossRef]
7. El-Sayed, S.A.; Khairy, M. Effect of heating rate on the chemical kinetics of different biomass pyrolysis materials. *Biofuels* **2015**, *6*, 157–170. [CrossRef]
8. Naqvi, S.R.; Tariq, R.; Hameed, Z.; Ali, I.; Taqvi, S.A.; Naqvi, M.; Niazi, M.; Noor, T.; Farooq, W. Pyrolysis of high-ash sewage sludge: Thermo-kinetic study using TGA and artificial neural networks. *Fuel* **2018**, *233*, 529–538. [CrossRef]
9. Taleb, D.A.; Hamid, H.A.; Deris, R.R.R.; Zulkifli, M.; Khalil, N.A.; Ahmad Yahaya, A.N. Insights into pyrolysis of waste tire in fixed bed reactor: Thermal behavior. *Mater. Today Proc.* **2020**, *31*, 178–186. [CrossRef]
10. Wulandari, Y.R.; Chen, S.S.; Hermosa, G.C.; Hossain, M.S.A.; Yamauchi, Y.; Ahamad, T.; Alshehri, S.M.; Wu, K.C.W.; Wu, H.-S. Effect of N2 flow rate on kinetic investigation of lignin pyrolysis. *Environ. Res.* **2020**, *190*, 109976. [CrossRef]
11. Brownsort, P.A. Biomass pyrolysis processes: Review of scope, control and variability. *UK Biochar Res. Cent. Lond.* **2009**, *1*, 1–39.
12. Mahmood, H.; Shakeel, A.; Abdullah, A.; Khan, M.I.; Moniruzzaman, M. A comparative study on suitability of model-free and model-fitting kinetic methods to non-isothermal degradation of lignocellulosic materials. *Polymers* **2021**, *13*, 2504. [CrossRef] [PubMed]
13. Mian, I.; Li, X.; Jian, Y.; Dacres, O.D.; Zhong, M.; Liu, J.; Ma, F.; Rahman, N. Kinetic study of biomass pellet pyrolysis by using distributed activation energy model and Coats Redfern methods and their comparison. *Bioresour. Technol.* **2019**, *294*, 122099. [CrossRef]
14. Chen, L.; Hu, J.; Han, Q.; Xie, A.; Zhou, Z.; Yang, J.; Tang, Q.; Mi, B.; Wu, F. Application of distributed activation energy model and Coats-Redfern integration method in the study of industrial lignin pyrolysis kinetics. *Biomass Convers. Biorefinery* **2022**, *15*, 21839–21849. [CrossRef]
15. Naqvi, S.R.; Tariq, R.; Hameed, Z.; Ali, I.; Naqvi, M.; Chen, W.-H.; Ceylan, S.; Rashid, H.; Ahmad, J.; Taqvi, S.A. Pyrolysis of high ash sewage sludge: Kinetics and thermodynamic analysis using Coats-Redfern method. *Renew. Energy* **2019**, *131*, 854–860. [CrossRef]
16. Castro Mur, D.; Yepes, D.M. *Integrating Characterization, Kinetic, and Thermodynamic Analysis into Pacific Colombian Biomass Residues for Preliminary Bioenergy Assessment Via Coats–Redfern Modeling Under Single-Rate Tga Conditions*; SSRN Library: Rochester, NY, USA, 2025.
17. Ogbuka, C.E.; Saud, P.; Yáñez, M.; Parajuli, R.; Godar Chhetri, S.; Pelkki, M. Harnessing loblolly pine (Pinus taeda L.) for sustainable biofuels and bioenergy: A review of biomass feedstock potential, conversion technologies, and forest management in the US. *Environ. Chall.* **2025**, *20*, 101246. [CrossRef]
18. Xiao, R.; Yang, W.; Cong, X.; Dong, K.; Xu, J.; Wang, D.; Yang, X. Thermogravimetric analysis and reaction kinetics of lignocellulosic biomass pyrolysis. *Energy* **2020**, *201*, 117537. [CrossRef]

19. Supee, A.H.; Zaini, M.A.A. Kinetics, thermodynamics, and thermal decomposition behavior of palm oil empty fruit bunch, coconut shell, bamboo, and cardboard pyrolysis: An integrated approach using Coats–Redfern method. *Environ. Monit. Assess.* **2023**, *195*, 1218. [CrossRef]
20. Demirbas, A. Relationships between heating value and lignin, moisture, ash and extractive contents of biomass fuels. *Energy Explor. Exploit.* **2002**, *20*, 105–111. [CrossRef]
21. Krotz, L.; Giazzi, G. *Elemental Analysis: CHNS/O Characterization of Carbon Black Compliance with ASTM D5373 Method*; Thermo Scientific: Waltham, MA, USA, 2017.
22. Fonseca, F.G.; Funke, A.; Niebel, A.; Dias, A.P.S.; Dahmen, N. Moisture content as a design and operational parameter for fast pyrolysis. *J. Anal. Appl. Pyrolysis* **2019**, *139*, 73–86. [CrossRef]
23. Chen, D.; Zheng, Y.; Zhu, X. In-depth investigation on the pyrolysis kinetics of raw biomass. Part I: Kinetic analysis for the drying and devolatilization stages. *Bioresour. Technol.* **2013**, *131*, 40–46. [CrossRef] [PubMed]
24. Chen, C.; Sun, K.; Huang, C.; Yang, M.; Fan, M.; Wang, A.; Zhang, G.; Li, B.; Jiang, J.; Xu, W. Investigation on the mechanism of structural reconstruction of biochars derived from lignin and cellulose during graphitization under high temperature. *Biochar* **2023**, *5*, 51. [CrossRef]
25. Urbanovici, E.; Popescu, C.; Segal, E. Improved iterative version of the Coats-Redfern method to evaluate non-isothermal kinetic parameters. *J. Therm. Anal. Calorim.* **1999**, *58*, 683–700. [CrossRef]
26. Wang, L.; Lei, H.; Liu, J.; Bu, Q. Thermal decomposition behavior and kinetics for pyrolysis and catalytic pyrolysis of Douglas fir. *RSC Adv.* **2018**, *8*, 2196–2202. [CrossRef]
27. Surahmanto, F.; Saptoadi, H.; Sulistyo, H.; Rohmat, T.A. Investigation of the pyrolysis characteristics and kinetics of oil-palm solid waste by using Coats–Redfern method. *Energy Explor. Exploit.* **2020**, *38*, 298–309. [CrossRef]
28. Al-Moftah, A.M.S.H.; Marsh, R.; Steer, J. Thermogravimetric Kinetic Analysis of Non-Recyclable Waste CO2 Gasification with Catalysts Using Coats–Redfern Method. *ChemEngineering* **2022**, *6*, 22. [CrossRef]
29. Polat, S.; Apaydin-Varol, E.; Pütün, A.E. Thermal decomposition behavior of tobacco stem Part I: TGA–FTIR–MS analysis. *Energy Sources Part A Recovery Util. Environ. Eff.* **2016**, *38*, 3065–3072. [CrossRef]
30. Emiola-Sadiq, T.; Zhang, L.; Dalai, A.K. Thermal and Kinetic Studies on Biomass Degradation via Thermogravimetric Analysis: A Combination of Model-Fitting and Model-Free Approach. *ACS Omega* **2021**, *6*, 22233–22247. [CrossRef]
31. El-Sayed, S.A.; Khass, T.M.; Mostafa, M.E. Thermal degradation behaviour and chemical kinetic characteristics of biomass pyrolysis using TG/DTG/DTA techniques. *Biomass Convers. Biorefinery* **2024**, *14*, 17779–17803. [CrossRef]
32. Ojha, D.K.; Viju, D.; Vinu, R. Fast pyrolysis kinetics of lignocellulosic biomass of varying compositions. *Energy Convers. Manag. X* **2021**, *10*, 100071. [CrossRef]
33. SriBala, G.; Carstensen, H.H.; Van Geem, K.M.; Marin, G.B. Measuring biomass fast pyrolysis kinetics: State of the art. *Wiley Interdiscip. Rev. Energy Environ.* **2019**, *8*, e326. [CrossRef]
34. Balci, S.; Dogu, T.; Yucel, H. Pyrolysis kinetics of lignocellulosic materials. *Ind. Eng. Chem. Res.* **1993**, *32*, 2573–2579. [CrossRef]
35. Chen, Z.; Hu, M.; Zhu, X.; Guo, D.; Liu, S.; Hu, Z.; Xiao, B.; Wang, J.; Laghari, M. Characteristics and kinetic study on pyrolysis of five lignocellulosic biomass via thermogravimetric analysis. *Bioresour. Technol.* **2015**, *192*, 441–450. [CrossRef]
36. Acharjee, T.C.; Coronella, C.J.; Vasquez, V.R. Effect of thermal pretreatment on equilibrium moisture content of lignocellulosic biomass. *Bioresour. Technol.* **2011**, *102*, 4849–4854. [CrossRef] [PubMed]
37. He, C. Biomass and Municipal Solid Waste (Msw) Pyrolysis in a Bench-Scale Drop Tube Reactor. Master's Thesis, University of Calgary, Calgary, AB, Canada, 2023.
38. Zheng, Y.; Tao, L.; Yang, X.; Huang, Y.; Liu, C.; Zheng, Z. Comparative study on pyrolysis and catalytic pyrolysis upgrading of biomass model compounds: Thermochemical behaviors, kinetics, and aromatic hydrocarbon formation. *J. Energy Inst.* **2019**, *92*, 1348–1363. [CrossRef]
39. Cho, J.; Chu, S.; Dauenhauer, P.J.; Huber, G.W. Kinetics and reaction chemistry for slow pyrolysis of enzymatic hydrolysis lignin and organosolv extracted lignin derived from maplewood. *Green Chem.* **2012**, *14*, 428–439. [CrossRef]
40. Tariq, R.; Saeed, S.; Riaz, M.; Saeed, S. Kinetic and thermodynamic evaluation of almond shells pyrolytic behavior using Coats–Redfern and pyrolysis product distribution model. *Energy Sources Part A Recovery Util. Environ. Eff.* **2023**, *45*, 4446–4462. [CrossRef]
41. Raza, M.; Abu-Jdayil, B.; Inayat, A. Pyrolytic kinetics and thermodynamic analyses of date seeds at different heating rates using the Coats–Redfern method. *Fuel* **2023**, *342*, 127799. [CrossRef]
42. Dong, Z.; Bai, X.; Xu, D.; Li, W. Machine learning prediction of pyrolytic products of lignocellulosic biomass based on physico-chemical characteristics and pyrolysis conditions. *Bioresour. Technol.* **2023**, *367*, 128182. [CrossRef]
43. Soria-Verdugo, A.; Goos, E.; García-Hernando, N. Effect of the number of TGA curves employed on the biomass pyrolysis kinetics results obtained using the Distributed Activation Energy Model. *Fuel Process. Technol.* **2015**, *134*, 360–371. [CrossRef]
44. Mabuda, A.I.; Mamphweli, N.S.; Meyer, E.L. Model free kinetic analysis of biomass/sorbent blends for gasification purposes. *Renew. Sustain. Energy Rev.* **2016**, *53*, 1656–1664. [CrossRef]

45. Pattanayak, S.; Hauchhum, L.; Loha, C.; Sailo, L.; Mishra, L. Experimental investigation on pyrolysis kinetics, reaction mechanisms and thermodynamic parameters of biomass and tar in N2 atmosphere. *Sustain. Energy Technol. Assess.* **2021**, *48*, 101632. [CrossRef]
46. Song, F.; Wang, X.; Li, T.; Zhang, J.; Bai, Y.; Xing, B.; Giesy, J.P.; Wu, F. Spectroscopic analyses combined with Gaussian and Coats-Redfern models to investigate the characteristics and pyrolysis kinetics of sugarcane residue-derived biochars. *J. Clean. Prod.* **2019**, *237*, 117855. [CrossRef]
47. Zhu, F.; Feng, Q.; Xu, Y.; Liu, R.; Li, K. Kinetics of pyrolysis of ramie fabric wastes from thermogravimetric data. *J. Therm. Anal. Calorim.* **2015**, *119*, 651–657. [CrossRef]
48. Kumar, A.A.; Kumar, R.; Ansari, A.A.; Kumar, R. Non-isothermal Degradation Analysis of Plywood and Determination of Kinetic Parameters Using Coats–Redfern Method. *J. Inst. Eng. (India) Ser. E* **2021**, *102*, 249–255. [CrossRef]
49. Wang, S.; Lin, H.; Ru, B.; Dai, G.; Wang, X.; Xiao, G.; Luo, Z. Kinetic modeling of biomass components pyrolysis using a sequential and coupling method. *Fuel* **2016**, *185*, 763–771. [CrossRef]
50. Postawa, K.; Fałtynowicz, H.; Szczygieł, J.; Beran, E.; Kułażyński, M. Analyzing the kinetics of waste plant biomass pyrolysis via thermogravimetry modeling and semi-statistical methods. *Bioresour. Technol.* **2022**, *344*, 126181. [CrossRef]
51. Ali, S.; Hussain, S.A.; Tohir, M.Z.M.; Nuruddin, A.A. Investigation of kinetic decomposition characteristics of Malaysian wood species using Coats and Redfern (CR) method. *Mater. Today Proc.* **2021**, *42*, 178–185. [CrossRef]